Research Square

Preprints are preliminary reports that have not undergone peer review.
They should not be considered conclusive, used to inform clinical practice,
or referenced by the media as validated information.

Dynamic bond reconfiguration drives crack-tip carbon migration to strengthen iron grain boundaries

Kazuma Ito

ito.nn3.kazuma@jp.nipponsteel.com

Nippon Steel Corporation

Takashi Otaki

Nippon Steel Corporation

Yuta Yoshimoto

Fujitsu Limited

Naoki Matsumura

Fujitsu Limited

Article

Keywords:

Posted Date: July 22nd, 2026

DOI: https://doi.org/10.21203/rs.3.rs-10085460/v1

License: This work is licensed under a Creative Commons Attribution 4.0 International License.
Read Full License

Additional Declarations: No competing interests reported.

Dynamic bond reconfiguration drives crack-tip carbon migration to strengthen iron grain boundaries

Kazuma Ito [a, *], Takashi Otaki [a], Yuto Yoshimoto [b], Naoki Matsumura [b]

[a] Advanced Technology Research Laboratories, Nippon Steel Corporation, 20-1 Shintomi, Futtsu, Chiba 293-8511, Japan

[b] Fujitsu Research, Fujitsu Limited, 4-1-1 Kamiodanaka, Nakahara-ku, Kawasaki, Kanagawa 211-8588, Japan

* Corresponding author. Advanced Technology Research Laboratories, Nippon Steel Corporation, 20-1 Shintomi, Futtsu, Chiba 293-8511, Japan

Email: ito.nn3.kazuma@jp.nipponsteel.com (K. Ito)

Abstract

Developing stronger alloys is essential for structural applications, but their reliability is limited by brittle cracking along general grain boundaries (GGBs). Solute segregation can control grain-boundary fracture, yet its effects are typically interpreted in terms of static cohesion changes before and after interfacial separation. How trace solutes modify moving-crack resistance at GGBs remains unclear because realistic segregation and crack propagation are difficult to treat atomistically. Here, we develop a fast and transferable Fe–C machine-learning interatomic potential. Using simulations of experimentally consistent carbon-segregated α-Fe GGBs, we show that trace carbon markedly increases crack-growth resistance, consistent with observed transition from intergranular fracture to cleavage. Carbon follows the moving crack tip through repeated breaking and reforming of Fe–C bonds, enriching the crack-tip region. We term this process dynamic bond reconfiguration (DBR). DBR dynamically amplifies static cohesive strengthening, revealing dynamic solute–crack-tip interactions as a framework for controlling brittle fracture in alloys.

Main

Intergranular fracture is a representative mode of brittle failure in metals and limits the reliability of structural materials in degradation phenomena such as hydrogen embrittlement[1-4] and liquid-metal embrittlement[5-7]. The need for lighter, more resource-efficient and longer-lasting structural materials drives further strengthening[1,8], but strengthening often increases susceptibility to intergranular fracture[2,6], and cracking along grain boundaries frequently becomes a dominant fracture path in high-strength alloys[9,10]. Understanding the atomistic mechanisms governing intergranular fracture and controlling them through solute elements are therefore central challenges in designing reliable structural materials.

In a simplified energetic description, grain-boundary fracture resistance can be expressed in terms of the ideal work of separation, W_{sep}, required to separate a grain boundary into two free surfaces without plastic deformation, and the additional work associated with processes near the crack tip[11-13]. The former represents the static strength of grain-boundary bonding and is often treated as the grain-boundary cohesive energy, or $2\gamma_{\mathrm{int}}$. The latter has conventionally been discussed as the plastic work, g_p, associated with plastic strain, dislocation emission, and slip near the crack tip. Solute-induced changes in W_{sep} have been widely discussed using the Rice–Wang model[14], which evaluates strengthening or embrittling effects from the difference between solute stabilization of the grain-boundary and fracture-surface states. This static thermodynamic framework has successfully explained whether segregating solutes strengthen or embrittle grain boundaries[15-17].

Importantly, this success does not imply that the additional crack-tip work contributing to effective fracture resistance can be neglected. Rather, in the classical picture, grain-boundary cohesion controls the competition between bond rupture and plastic relaxation at the crack tip and can thereby influence the plastic work, g_p[13,18,19]. Thus, W_{sep}, or $2\gamma_{\mathrm{int}}$, remains a central descriptor for understanding solute-induced grain-boundary strengthening and embrittlement, even when plastic work accounts for a large fraction of the total effective fracture resistance. At the same time, W_{sep} is a static quantity defined from relaxed atomic structures before and after separation, and it does not directly describe solute enrichment, atomic rearrangement, or bond breaking and reforming near a crack tip advancing under a strong stress gradient.

Carbon is a particularly important solute for testing the validity and limitations of this static cohesion picture. In Fe–C alloys, even ppm-level carbon markedly segregates to grain boundaries in α-Fe[20]. Low-temperature fracture tests of ultra-low-carbon steels have further shown that trace carbon suppresses intergranular fracture and promotes cleavage fracture[21,22]. This behaviour is consistent with a carbon-induced increase in static grain-boundary cohesion within the Rice–Wang picture[17]. In addition, carbon is a small interstitial solute that can sensitively segregate to open local structures, such as grain boundaries and crack tips, and can modify local bonding networks through Fe–C bonds[23]. The Fe–C system therefore provides a useful model for examining not only how segregating solutes statically stabilize grain boundaries before fracture but also how they alter local bonding states near an advancing crack tip.

Atomistic analysis of this problem faces two major challenges. First, high-angle random grain boundaries, which are common in practical polycrystals and are hereafter referred to as general grain boundaries, consist of diverse and complex local atomic structures without special crystallographic symmetry. Therefore, constructing an interatomic potential that describes, with consistent accuracy, the atomic environments that appear during carbon segregation, deformation, and fracture is difficult[24]. Second, directly tracking crack propagation across multiple general grain boundaries with experimentally relevant carbon segregation states requires large-scale and long-timescale atomistic simulations. Although first-principles calculations provide high reliability for individual atomic structures, their accessible system sizes and timescales are too limited to systematically treat equilibrium segregation and crack propagation at diverse general grain boundaries.

Here, we overcome these challenges by constructing a fast and transferable Fe–C machine-learning interatomic potential (MLIP) and using it to analyse carbon segregation and crack propagation at general grain boundaries. Using grand-canonical Monte Carlo/molecular dynamics (GCMC/MD) [25], we reproduced experimentally consistent carbon segregation states and performed crack-propagation simulations for multiple carbon-segregated general grain boundaries. We find that carbon segregation systematically increases the effective crack-growth resistance. This increase correlates with the static Rice–Wang-type cohesion change but exceeds the static prediction in magnitude. Atomistic analysis shows that carbon near the crack tip follows the advancing crack by dynamically breaking and reforming Fe–C bonds. We term this process dynamic bond

reconfiguration (DBR). DBR dynamically amplifies the static grain-boundary strengthening contribution through local carbon enrichment and Fe–C bond reconfiguration at the moving crack tip. These results show that grain-boundary fracture resistance can be controlled not only by static ideal separation work but also by the dynamic evolution of solute distributions and bonding networks at advancing crack tips.

Results

In this study, we atomistically evaluated the crack-growth resistance of carbon-segregated general grain boundaries in the Fe–C system, in which trace carbon addition has been reported to change the low-temperature fracture mode from intergranular fracture along general grain boundaries to cleavage[21,22]. In the reference experiments, fracture at 171 K occurred mainly along general grain boundaries when almost no carbon was present in solid solution, with the intergranular fracture ratio reaching 74%. By contrast, when approximately 20 wt ppm carbon was present in solid solution, the fracture surface became almost entirely cleavage[21,22]. However, these experiments did not directly measure the amount of carbon segregated to general grain boundaries. We therefore first validated the segregation calculations under a condition corresponding to a bulk carbon concentration of 60 wt ppm, for which the carbon interfacial excess at general grain boundaries has been reported using atom probe tomography[20]. Using the same approach, we then constructed carbon-segregated general grain-boundary models corresponding to a bulk carbon concentration of 20 wt ppm and examined

how trace carbon segregation under the experimental fracture-transition condition affects grain-boundary crack-growth resistance.

A fast and transferable Fe–C MLIP for general grain-boundary segregation and fracture

To analyse carbon segregation and crack propagation at general grain boundaries, we constructed a fast and transferable Fe–C MLIP using the Generator of Neural Network Interatomic Potential for Molecular Dynamics (GeNNIP4MD) workflow[26], which sampled configurations relevant to segregation, deformation, and fracture. The final dataset contained 27,723 structures and 1,394,289 local atomic environments and was used to train an MLIP in the performant implementation of the atomic cluster expansion (PACE) [27,28] format. Details of the DFT calculations, GeNNIP4MD workflow and MLIP training are provided in Supplementary Note 1.

As shown in Fig. 1a–c, the resulting MLIP accurately reproduced carbon segregation at general grain boundaries, C–C interactions, and the cohesive energy of carbon-segregated grain boundaries in α-Fe, with accuracy comparable to or higher than that of an existing MLIP based on the Behler–Parrinello neural network potential (BNNP) framework[29]. We further evaluated the local extrapolation grade[30] of atomic environments generated during crack-propagation simulations and found no environments with an extrapolation grade above 2, the usual threshold for additional training (Fig. 1d). The computational speed was approximately ten times higher than that of BNNP and was of the same order as those of empirical interatomic potentials, such as the bond-order

potential (BOP)[31] and modified embedded-atom method (MEAM)[32] (Fig. 1e). Additional MLIP validation is provided in Supplementary Note 2. These results indicate that the present MLIP is suitable for both GCMC/MD segregation calculations and large-scale crack-propagation simulations.

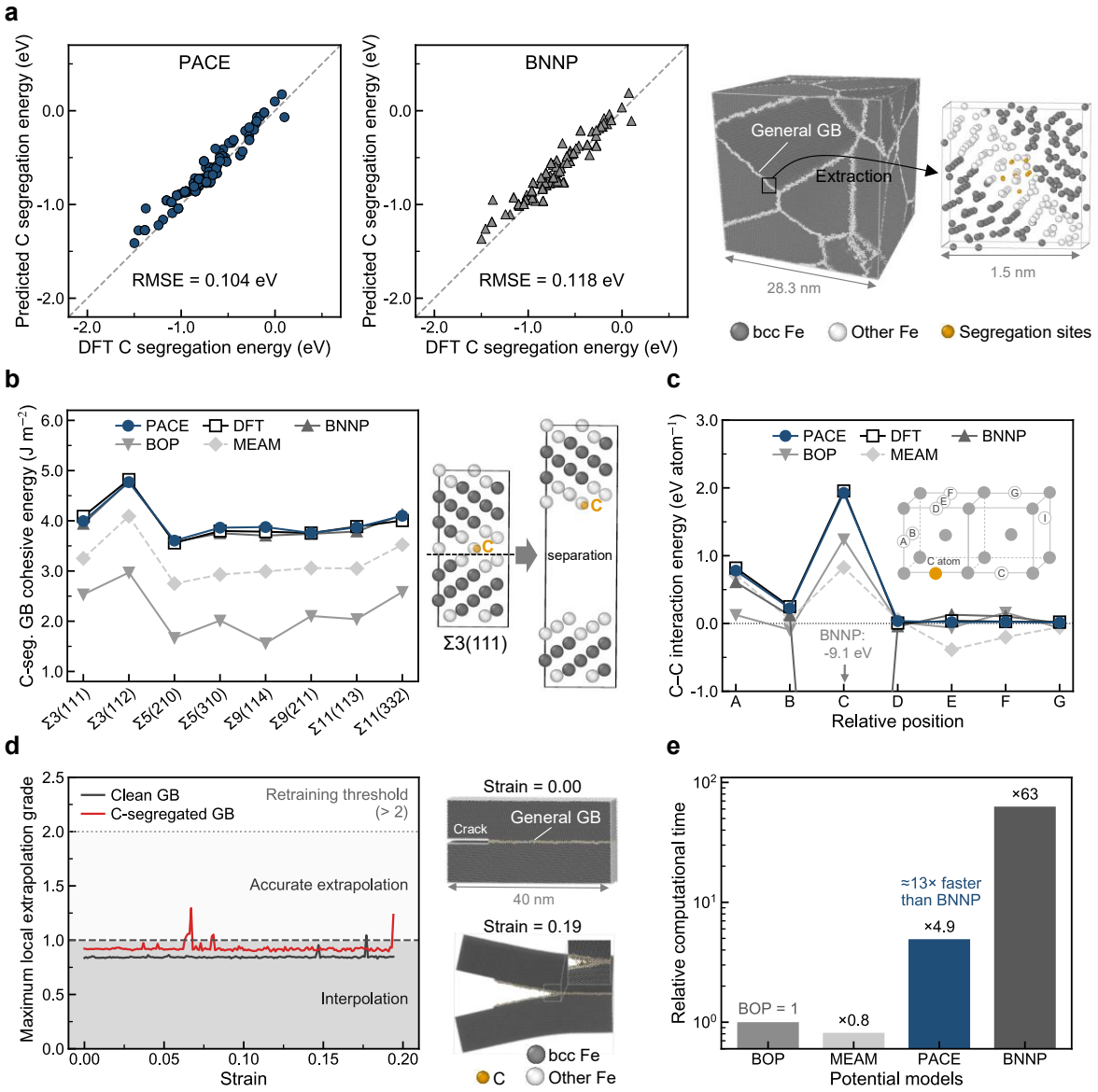


Fig. 1: Accuracy, transferability, and computational efficiency of the Fe–C MLIP. **a,** Comparison with DFT of C segregation energies at general grain boundaries extracted from nanopolycrystalline models with random grain orientations. **b,** Comparison of cohesive energies of symmetric tilt grain boundaries with C segregated to the most stable site. The schematic shows the atomic structure used for the Σ3(111) symmetric tilt grain-boundary calculation. **c,** Comparison of C–C interaction energies in α-Fe. The inset shows the relative positions of the reference C atom and the second C atom. **d,** Maximum local extrapolation grade at each strain for atomic environments generated during crack-propagation simulations of the general grain boundary analysed in Fig. 4**.** The right panels show representative atomic structures before and after crack propagation. **e,** Relative computational time of each interatomic potential evaluated on Fugaku, normalized by that of BOP. Overall, PACE reproduces DFT trends for C segregation at general grain boundaries, grain-boundary cohesion, and C–C interactions, including the strong repulsion between neighbouring C atoms. The maximum extrapolation grade remains below the threshold for additional training during crack propagation, indicating that the generated atomic environments are within the applicability domain of the MLIP. PACE is also substantially faster than BNNP and achieves computational efficiency comparable to empirical interatomic potentials. DFT, density functional theory; RMSE, root-mean-square error; GB, grain boundary.

GCMC/MD analysis with the MLIP quantitatively predicts carbon segregation at general grain boundaries

Next, we constructed bicrystal models containing 12 general grain boundaries. These boundaries had misorientation angles of 18.2°–48.5° and grain-boundary energies of 1.56–1.86 J m^{-2}. Using the same MLIP, we evaluated general grain boundaries in nanopolycrystalline models and obtained an average grain-boundary energy of 1.58 J m^{-2}, in good agreement with the experimentally estimated energy of general grain boundaries, 1.63 J m^{-2} (Fig. 2a)[33]. The grain-boundary energies of the bicrystal models also fell within the energy distribution of high-angle grain boundaries in the nanopolycrystalline models (Fig. 2a). These results confirm that the bicrystal models represent general grain boundaries in polycrystalline materials.

Fig. 2b shows carbon segregation states at general grain boundaries obtained by GCMC/MD using the chemical potential corresponding to a bulk carbon concentration of 60 wt ppm at 373 K. The relationship between the chemical potential and the bulk carbon concentration is provided in Supplementary Note 3. Representative grain boundaries with the maximum, minimum, and average segregation amounts are shown. Carbon was strongly localized within approximately 2.5 Å of the grain-boundary centre, with the local concentration reaching up to approximately 30 at.%. As shown in Fig. 2c, the average interfacial excess and standard deviation obtained for the 12 general grain boundaries were in good agreement with the experimental values[20]. This demonstrates that the present MLIP combined with GCMC/MD can quantitatively predict carbon segregation at general grain boundaries. Further analysis of the Voronoi volume and coordination number of segregated

carbon showed that carbon mainly occupied open grain-boundary sites corresponding to coordination numbers of 6 and 7, which were larger than the octahedral sites in bulk α-Fe (Fig. 2d,e).

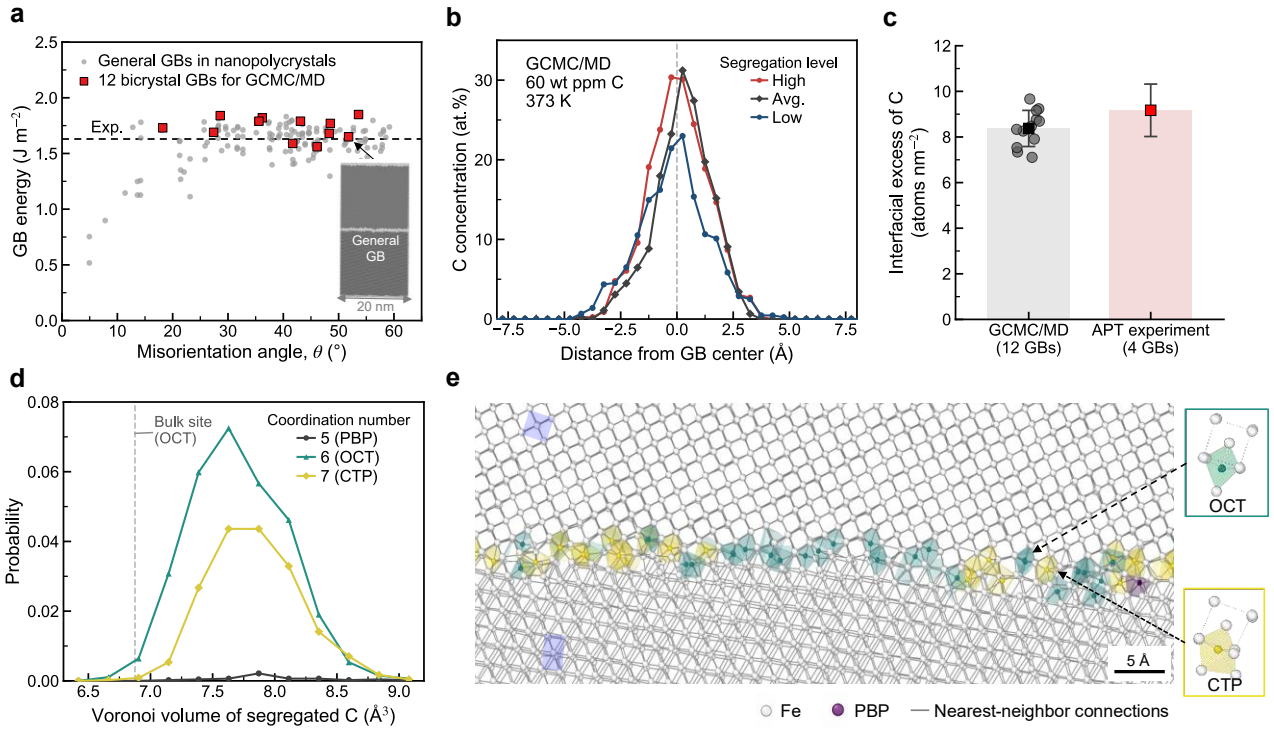


Fig. 2: Quantitative prediction of carbon segregation at general grain boundaries by GCMC/MD and the local structure of segregation sites.

a, Relationship between grain-boundary energy and misorientation angle for the 12 general grain-boundary bicrystal models used in this study. The energy distribution of high-angle grain boundaries in nanopolycrystalline models with random grain orientations and the experimentally estimated energy of general grain boundaries are shown for comparison. The inset shows a representative general grain-boundary model.

b, Carbon concentration profiles normal to representative general grain boundaries obtained by GCMC/MD using the chemical potential corresponding to a bulk carbon concentration of 60 wt ppm at 373 K. Grain boundaries with the maximum, minimum, and average segregation amounts are shown. Carbon is localized near the grain-boundary centre, with the local concentration reaching up to approximately 30 at.%.

c, Calculated carbon interfacial excess for the 12 general grain boundaries compared with atom-probe tomography measurement**s.** The quantitative agreement demonstrates that GCMC/MD predicts carbon segregation at general grain boundaries. Error bars represent standard deviations among the 12 calculated grain boundaries and four measured grain boundaries.

d, Probability density distribution of Voronoi volumes for grain-boundary-segregated carbon classified by coordination number. Carbon mainly occupies distorted octahedral sites (OCT) and capped trigonal prism sites (CTP), both with larger Voronoi volumes than octahedral sites in bulk α-Fe. PBP denotes a pentagonal bipyramid site.

e, Atomic structures of carbon segregation sites at a representative general grain boundary. OCT and CTP local environments are shown in different colours.

Carbon segregation increases crack-growth resistance beyond static cohesion changes

Fig. 3a shows a representative model used for the crack-propagation simulations (Supplementary Video 1). Clean and C-segregated bicrystal models obtained by GCMC/MD were replicated fourfold along the crack-propagation direction, an edge crack was introduced, and tensile strain was applied normal to the grain-boundary plane. The strain rate was 1×10^9 s^{-1}. The simulations were initiated at 1 K to suppress thermally activated carbon diffusion and thermally assisted dislocation emission, thereby isolating brittle crack propagation. Under these conditions, the average crack velocity in a representative case was approximately 100 m s^{-1}, corresponding to the lower end of reported brittle crack velocities in steels[34]. In the stress–strain curve of a representative grain boundary, the stress in the clean model reached a maximum at a strain of 0.026 and then dropped sharply as the crack propagated (Fig. 3b). In contrast, in the C-segregated grain boundary, crack propagation started at a similar strain, but the stress increased again and reached a maximum at a strain of approximately 0.045. This indicates that C segregation markedly increases resistance after crack initiation rather than the crack-initiation stress itself.

Crack-growth resistance was evaluated as $\mathrm{d}U/\mathrm{d}A$ from the relationship between internal energy U and one-sided crack area A. After excluding the initial burst region, U increased almost linearly with A, and the fitted slope was taken as $\mathrm{d}U/\mathrm{d}A$ (Fig. 3c). In this steady crack-growth regime, residual elastic strain energy is expected to contribute mainly as an A-independent term. Because A is defined for one fracture surface, ideal cleavage is expected to yield $\mathrm{d}U/\mathrm{d}A = 2\gamma$; for Fe(001)

cleavage, $\mathrm{d}U/\mathrm{d}A = 5.08$ J m^{-2}, in good agreement with 2γ from the PACE-calculated surface energy, γ =2.53 J m^{-2} (Fig. 3d). The average resistance of clean general grain boundaries was 4.60 J m^{-2}, below the Fe(001) cleavage value, whereas carbon segregation states corresponding to a bulk carbon concentration of 20 wt ppm increased the average resistance to 7.80 J m^{-2}, exceeding the cleavage value. Individual results are provided in Supplementary Note 4. This trend is consistent with experiments showing that trace carbon suppresses intergranular fracture and promotes cleavage[21,22], although the comparison evaluates relative crack-growth resistance under dislocation-free atomistic conditions rather than quantitative experimental fracture energies including plastic work, g_p.

To clarify the origin of the C-induced resistance increase, we separated it into a static Rice–Wang-type contribution, evaluated from pre- and post-fracture structures, and an excess contribution beyond this static term (Fig. 3d and Supplementary Note 5). The static contribution accounted for only about half of the observed increase in $\mathrm{d}U/\mathrm{d}A$. A grain-boundary-by-grain-boundary comparison further showed that the Rice–Wang-type evaluation captured the strengthening trend semi-quantitatively but underestimated its magnitude by approximately a factor of two (Fig. 3e). Thus, a dynamic contribution emerging during crack propagation is essential for the C-induced increase in crack-growth resistance.

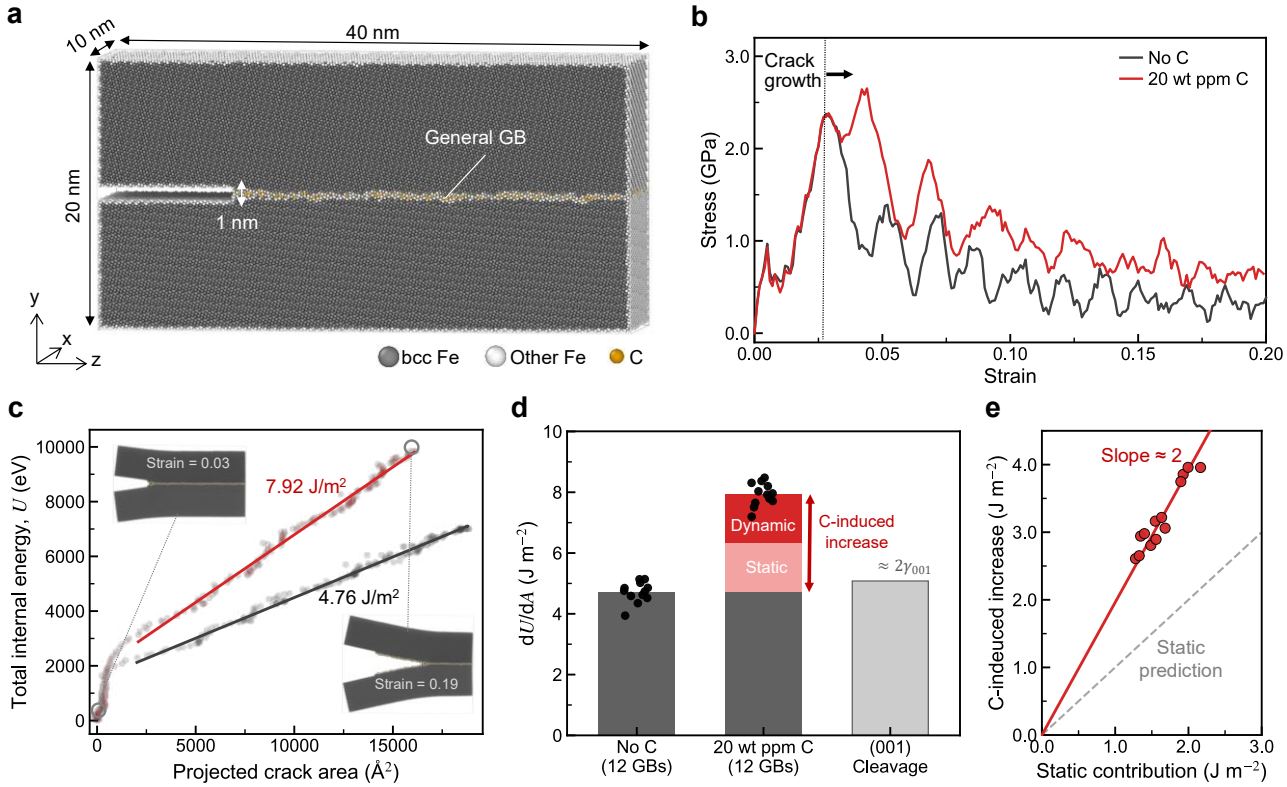


Fig. 3: Carbon segregation increases crack-growth resistance beyond the static contribution.

a, Representative C-segregated general grain-boundary model used for the crack-propagation simulations. An edge crack was introduced along the C-segregated grain boundary, and tensile deformation was applied normal to the grain-boundary plane along the y direction.

b, Stress–strain curves for a representative grain boundary. The clean grain boundary shows a sharp stress drop after crack initiation, whereas the grain boundary with C segregation corresponding to a bulk carbon concentration of 20 wt ppm shows stress re-increase after crack initiation, indicating increased crack-growth resistance.

c, Relationship between internal energy, U, and one-sided crack area, A, for the same representative grain boundary. Crack-growth resistance, dU/dA, was evaluated from the slope of the linear region after the initial burst. C segregation markedly increases the slope.

d, Average crack-growth resistance for 12 general grain boundaries. Clean general grain boundaries fall below $2\gamma_{001}$ for Fe(001) cleavage, whereas C-segregated grain boundaries exceed it. The C-induced increase is shown as the static Rice–Wang-type contribution, evaluated from structures before and after fracture, and the excess beyond this contribution. Black points denote individual grain boundaries.

e, Relationship between the C-induced increase in crack-growth resistance and the static Rice–Wang-type contribution for each grain boundary. The red line shows a linear fit, and the dashed line indicates the case where the total increase is fully explained by the static contribution. The increase exceeds the static prediction, demonstrating the importance of a dynamic contribution during crack propagation.

Dynamic bond reconfiguration increases crack-growth resistance through carbon enrichment at crack tips

To identify the origin of this dynamic contribution, we analysed atomistic structural changes during crack propagation in a C-segregated grain boundary. For a representative grain boundary, we tracked the coordination number, Voronoi volume, and local bonding state of two segregated carbon atoms, denoted C atom 1 and C atom 2, hereafter referred to as C1 and C2, respectively. For C1, the Voronoi volume increased as the crack approached, followed by a decrease in coordination number and rupture of Fe–C bonds; the carbon atom was then left on the newly formed surface (Fig. 4a,b). This behaviour is consistent with the Rice–Wang-type picture, in which segregated solutes transfer to fracture surfaces upon separation.

C2 exhibited a distinct behaviour. After its Fe–C bonds were initially broken, C2 did not remain on the fracture surface, but migrated in the crack-propagation direction while rebonding with newly exposed Fe atoms near the crack tip (Fig. 4a,b and Supplementary Video 2). The local structure at strains of 0.068–0.070 shows that Fe–C bonds behind the crack tip and Fe–Fe bonds near C were broken, whereas new bonds formed with Fe atoms ahead of the advancing crack (right panels in Fig. 4b). Thus, carbon atoms can follow the moving crack tip through repeated bond breaking and reforming. We further analysed the displacement component along the crack-propagation direction for carbon atoms initially located in the crack-propagation region. Approximately 60% moved preferentially in the crack-propagation direction, with a maximum displacement of approximately 20

Å and an average displacement of approximately 2.0 Å (Supplementary Note 6). This average displacement is comparable to the C2 migration distance between strains of 0.068 and 0.070 in Fig. 4b. Because the simulation temperature was 1 K, this motion is not thermally activated diffusion but rather a non-equilibrium transport process driven by the crack-tip stress field and local structural changes.

The carbon concentration near the crack tip increased from approximately 8.7 at.% in the unstrained state to approximately 17 at.% near the maximum stress (Fig. 4c). This enriched state persisted during crack propagation, and no pronounced carbon-depleted region appeared ahead of the crack tip. These results indicate that carbon was not supplied by long-range diffusion from the unbroken grain boundary but was instead rearranged from the already fractured region and retained near the crack tip.

We term this dynamic process, in which carbon follows the crack tip through repeated breaking and reforming of Fe–C bonds, dynamic bond reconfiguration (DBR). DBR approximately doubles the effective carbon concentration near the crack tip and increases the participation of Fe–C bonds in the local bonding network undergoing rupture and reformation. These results show that carbon segregation increases crack-growth resistance through both static cohesion changes and crack-tip carbon enrichment by DBR.

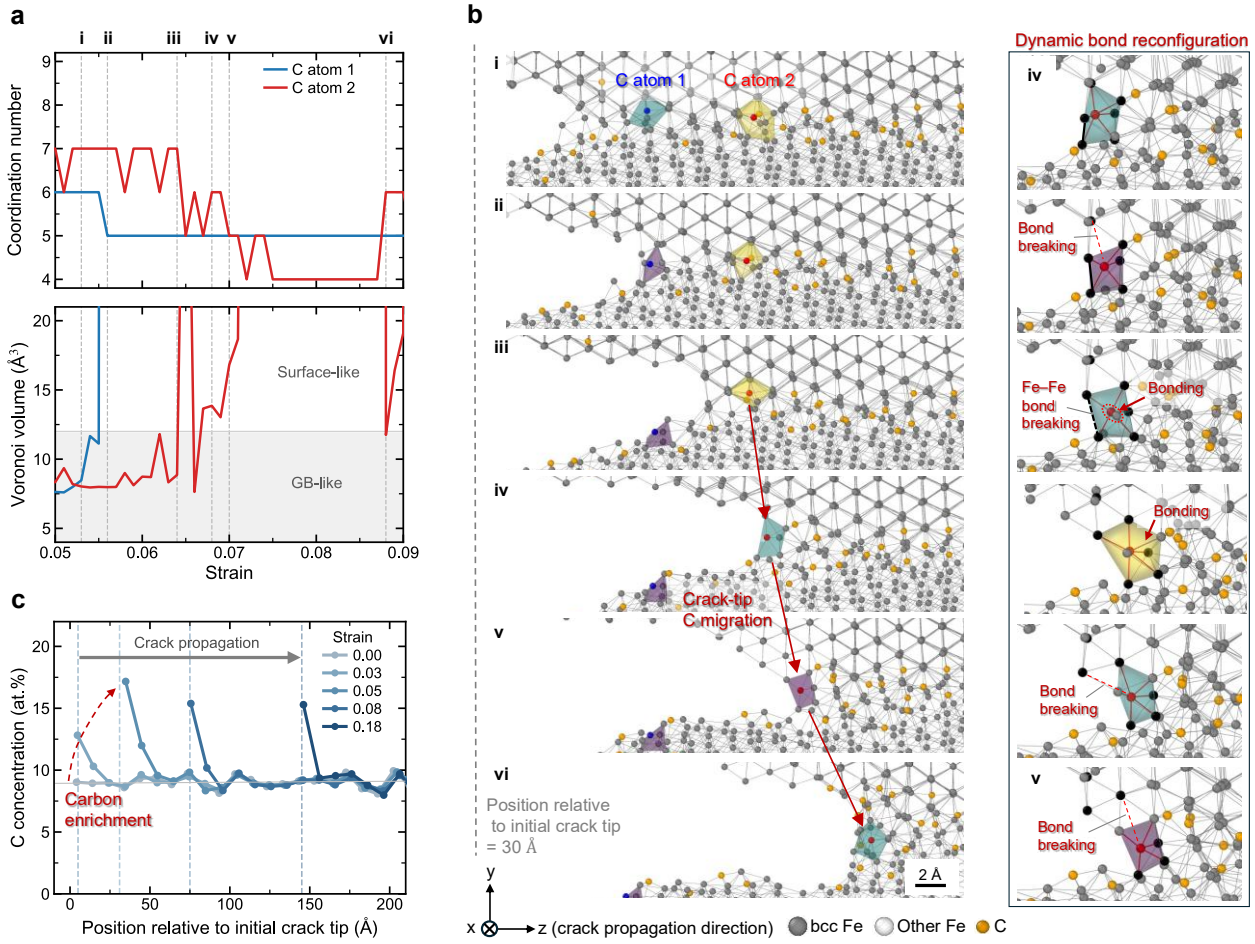


Fig. 4: Carbon enrichment at crack tips by dynamic bond reconfiguration.

a, Changes in the coordination number and Voronoi volume of two carbon atoms in a representative C-segregated general grain boundary. Dashed lines i–vi correspond to the atomic snapshots in **b**. The low- and high-Voronoi-volume regions indicate GB-like and surface-like local environments, respectively.

b, Structural evolution of C atom 1 and C atom 2 during crack propagation. C atom 1 is left on the fracture-surface side after bond rupture, whereas C atom 2 follows the moving crack tip. Polyhedra around C atom 1 and C atom 2 indicate the local coordination environments. The right panels magnify the region around C atom 2, showing rupture of Fe–C and Fe–Fe bonds behind the crack tip and rebonding with Fe atoms ahead of the crack. This continuous process of bond breaking and rebonding is termed dynamic bond reconfiguration.

c, Evolution of the C concentration profile along the crack-propagation direction. Dashed lines mark the crack-tip position at each strain. During crack propagation, DBR retains carbon near the crack tip and increases the local C concentration to approximately twice the initial grain-boundary concentration.

Discussion

In the present simulations, neither dislocation emission nor slip motion was observed during crack propagation. Thus, DBR is distinct from the conventional plastic work, g_p, which is usually associated with plastic strain, dislocation emission, and slip near the crack tip. Instead, DBR can be understood as a dynamic crack-tip contribution that increases the effective work required for crack propagation beyond the static ideal work of separation, W_{sep}, by reconstructing local bonding states during crack advance. This distinction does not imply that its contribution is small. Static grain-boundary cohesion, W_{sep} or $2\gamma_{\mathrm{int}}$, can also be small compared with the total effective fracture resistance, yet it can control the competition between bond rupture and plastic relaxation and thereby influence the much larger plastic work, g_p[13,18,19]. Similarly, DBR directly increases the effective crack-growth work under the present conditions through carbon enrichment and Fe–C bond reconfiguration at the advancing crack tip. At lower strain rates or when dislocation emission is allowed, DBR may also modify the competition between bond rupture and plastic relaxation and increase conventional plastic dissipation. The average crack velocity was within the reported range for brittle cracks in steels, and extrapolation-grade analysis confirmed that crack-propagation environments remained within the MLIP applicability domain. These results support the interpretation that DBR is not simply an artefact of excessive crack velocity or potential extrapolation.

DBR therefore does not replace the static cohesion change described by the Rice–Wang model.

Rather, it dynamically amplifies the static grain-boundary strengthening contribution, evaluated from relaxed structures before and after fracture, through local carbon enrichment and Fe–C bond reconfiguration during crack propagation. In this study, the C-induced increase in crack-growth resistance correlated with the static Rice–Wang-type contribution among grain boundaries, whereas its magnitude exceeded the static prediction (Fig. 3e). This suggests that the static cohesive effect per carbon atom governs the strengthening trend, while DBR increases the amount of carbon contributing to the cohesion change per unit crack area.

Carbon can exhibit DBR because it strongly segregates to grain boundaries, rearranges within open local structures as a small interstitial solute, and forms stable covalent Fe–C bonds with undercoordinated Fe atoms exposed during crack advance[23]. These properties allow carbon not merely to remain on newly formed surfaces but also to be retained near the crack tip and rearranged with the evolving bonding network. Similar DBR may occur for solutes that combine grain-boundary segregation, interstitial rearrangement, and covalent bonding with host-metal atoms. For example, B behaves as an interstitial solute in bcc Fe, segregates strongly to Fe grain boundaries, and forms stable covalent bonds with Fe[15], making it a promising candidate for DBR-mediated grain-boundary strengthening. Carbon-induced grain-boundary strengthening has also been reported in bcc transition metals such as Mo[35] and in NbMoTaW refractory high-entropy alloys[36], suggesting that these conditions are not unique to Fe–C. Conversely, grain-boundary-embrittling solutes such as P, which forms covalent bonds with Fe[15] and can adopt interstitial-like local configurations at grain

boundaries[37], may dynamically rearrange at crack tips in a way that amplifies reductions in grain-boundary cohesion. Thus, DBR is not limited to Fe–C strengthening but represents a broader class of dynamic solute–crack-tip interactions through which segregation can enhance or reduce fracture resistance, providing a framework for understanding and controlling brittle fracture in alloys where segregation governs fracture behaviour.

Methods

Construction and validation of the Fe–C machine-learning interatomic potential

To describe C segregation and crack propagation at general grain boundaries using a single interatomic potential, we constructed a fast and transferable MLIP for the Fe–C binary system. The training dataset was generated using the iterative GeNNIP4MD workflow[26], which consists of training, exploration, screening, and labelling steps. In this workflow, poorly learned structures are detected from prediction deviations among multiple preliminary MLIPs, and a second screening step based on structural similarity reduces redundancy while incorporating diverse atomic environments into the training dataset[38].

The initial training dataset consisted of (1) strained α-Fe containing solute carbon, (2) α-Fe containing C–vacancy clusters, (3) strained Fe carbides, including cementite and ε-carbide, (4) cementite containing point defects, (5) ε-carbide with various vacancy configurations, (6) strained diamond and graphene, and (7) Fe–Fe, Fe–C, and C–C dimers. The exploration targets included (1) strained α-Fe containing solute carbon, (2) α-Fe containing self-interstitial atoms, (3) α-Fe containing

vacancy clusters, small voids, and multiple carbon atoms, (4) low-index surfaces of α-Fe containing solute carbon, (5) strained symmetric tilt grain boundaries containing solute carbon, (6) generalized stacking faults in α-Fe containing solute carbon, (7) screw dislocations with segregated carbon, (8) cementite containing point defects, (9) low-index cementite surfaces, (10) generalized stacking faults in cementite, and (11) cementite/α-Fe interfaces. Exploration was performed at 300–1500 K and 0–5 GPa, and candidate structures were generated by MD and structural relaxation using preliminary MLIPs in the Large-scale Atomic/Molecular Massively Parallel Simulator (LAMMPS)[39].

In each GeNNIP4MD cycle, we used four Deep Potential (DP) MLIPs[40] trained with identical hyperparameters but different random seeds. DP models were used because data-parallel training with DeePMD-kit[40] enabled efficient execution of many iterative cycles. Structures with maximum force deviations of 0.15–0.35 eV $Å^{-1}$ among the four models were selected as candidates, and DFT labelling targets were then chosen by structural-similarity screening. DFT labelling calculations were performed using the Vienna Ab initio Simulation Package (VASP)[41,42] under conditions equivalent to those used in previous Fe and Fe–H binary MLIP studies[24,43,44]. After 75 iterations, the final training dataset contained 27,723 structures and 1,394,289 local atomic environments. The production model was trained in the PACE format using Pacemaker[27]. Details of the DFT calculations, GeNNIP4MD workflow, initial and explored structures, and DP and PACE training conditions are provided in Supplementary Note 1.

The accuracy of the constructed PACE model was evaluated against DFT calculations or reported

DFT data[45] for the basic properties of α-Fe, lattice defects, C solution energies, C–C interactions, vacancy–C interactions, dislocation–C interactions, C segregation energies at symmetric tilt and general grain boundaries, formation energies of Fe carbides, point defects in cementite, and generalized stacking-fault energies in cementite. Segregation energies at symmetric tilt and general grain boundaries were calculated following a previous method[44]. Previously reported BNNP[29], MEAM[32], and BOP[31] potentials were used for comparison. All interatomic-potential calculations were performed using LAMMPS[39].

To assess the applicability of the model to crack-propagation simulations, we evaluated the extrapolation grade[30] of atomic environments generated during crack propagation. The extrapolation grade is an active-learning-based metric that quantifies the similarity of each local atomic environment to environments included in the training dataset. Extrapolation grades of 0–1, 1–2, and 2–10 correspond to interpolation, high-accuracy extrapolation, and reliable extrapolation regions, respectively: the last denotes environments suitable for active-learning selection, not necessarily guaranteed prediction accuracy. Structures containing environments with grades above 2 are typically candidates for additional DFT labelling, whereas grades above 10 indicate configurations too far from the training domain to be reliable labelling candidates. Extrapolation-grade analysis is often used to validate large-scale systems for which direct DFT verification is impractical[24,43,44,46-48]. In this study, atomic structures were extracted every 0.001 strain from crack-propagation simulations of C-segregated general grain boundaries, and extrapolation grades were evaluated for all atoms.

Computational performance was evaluated following a previous method[44] using a $50 \times 50 \times 50$ α-Fe supercell. Because the number of C atoms in the present Fe–C systems is much smaller than that of Fe atoms, the computational cost is dominated by Fe. We therefore measured the wall-clock time per atom per MD step using a 250,000-atom α-Fe supercell at 300 K in the NVT ensemble. The benchmark was performed on the Fugaku supercomputer using two nodes equipped with 48-core A64FX processors to ensure sufficient memory.

Determination of carbon chemical potential and GCMC/MD segregation calculations

The carbon chemical potential used for grain-boundary segregation calculations was determined from the carbon insertion free energy in bulk α-Fe. In principle, the relationship between chemical potential and bulk carbon concentration can be obtained directly by GCMC/MD[25] in bulk systems. In the present system, however, the energy difference between the immediately inserted carbon atom at an octahedral site and the MD-relaxed state was large, making sufficient equilibration difficult within practical simulation times. We therefore evaluated the free energies of a $12 \times 12 \times 12$ α-Fe supercell and the same supercell containing one carbon atom at an octahedral site using nonequilibrium thermodynamic integration along the Frenkel–Ladd path[49]. The insertion free energy, ΔF_{ins}, was obtained from their difference.

The carbon chemical potential was then evaluated by adding the configurational entropy associated with octahedral-site occupation within an ideal lattice-gas approximation: $\mu_{\mathrm{C}} = \Delta F_{\mathrm{ins}} +$

$k_{\mathrm{B}}T \ln\left(\frac{x}{1-x}\right)$, where x is the octahedral-site occupancy. This relation was used to determine the chemical potentials corresponding to bulk carbon concentrations of 20 and 60 wt ppm. The relationship between chemical potential and bulk carbon concentration is shown in Supplementary Note 3. A $12 \times 12 \times 12$ supercell containing one carbon atom corresponds to approximately 60 wt ppm, and μ_{C} was confirmed to be sufficiently converged for supercells of $10 \times 10 \times 10$ or larger. The grain-boundary models were 12 bicrystal models containing general grain boundaries constructed using a previous method[45]. Their misorientation angles and grain-boundary energies were 18.2°–48.5° and 1.56–1.86 J m^{-2}, respectively, consistent with the distribution of high-angle grain boundaries in nanopolycrystalline models and the experimentally estimated energy of general grain boundaries[33]. Bicrystal and polycrystalline models were generated using Atomsk[50].

GCMC/MD hybrid calculations were performed at 373 K for each grain-boundary model using the chemical potential corresponding to a bulk carbon concentration of 60 wt ppm. In GCMC/MD, 100 MD relaxation steps were performed after every 500 carbon insertion/deletion attempts, with an MD timestep of 0.5 fs. GCMC/MD was continued until the segregation amount converged, corresponding to 1×10^7 MD steps, and the interfacial excess was evaluated from the final state. The carbon interfacial excess was calculated following the standard definition of interfacial excess by integrating the excess concentration obtained by subtracting the bulk carbon concentration from the carbon concentration profile normal to the grain boundary.

Crack-propagation simulations

Crack-propagation simulations were performed using the 12 general grain-boundary bicrystal models described above. Clean grain boundaries were compared with grain boundaries containing carbon segregation corresponding to a bulk carbon concentration of 20 wt ppm. The carbon segregation states were generated by GCMC/MD at 373 K. The average interfacial excess of the 12 grain boundaries was 8.07 atoms nm^{-2}, with minimum and maximum values of 6.76 and 9.28 atoms nm^{-2}, respectively.

Crack-propagation models were constructed by replicating each grain-boundary bicrystal four times along the crack-propagation direction. The resulting models were approximately 40, 20, and 10 nm in the crack-propagation, tensile, and periodic thickness directions, respectively. Periodic boundary conditions were applied along the thickness direction, whereas free surfaces were used along the crack-propagation and tensile directions. An edge crack was introduced along the grain boundary by removing atoms from one side of the model. The initial crack extended 10 nm along the crack-propagation direction and had an opening width of 1 nm along the tensile direction. The 1 nm-thick regions at the upper and lower ends along the tensile direction were used as loading layers. At each loading increment, a displacement corresponding to an average tensile strain of 0.1% was applied, followed by 1 ps of MD relaxation. The average strain rate was 1×10^{9} s^{-1}. Following the method proposed by Xu et al.[51], only the centre-of-mass position of each loading layer was constrained, whereas the relative displacements of individual atoms within the layer were not

constrained.

All MD relaxation after displacement loading was performed under NVE conditions without a thermostat. This excluded energy exchange with a heat bath and allowed external work to be reflected in the internal energy of the system. The initial temperature was 1 K, and the temperature increase during crack propagation was confirmed to be less than 10 K. No dislocation emission from the crack tip was observed under the present conditions. Atomic structures were visualized and analysed using OVITO[52].

Evaluation of crack-growth resistance and static Rice–Wang contribution

Crack-growth resistance was evaluated from the evolution of the one-sided crack area, A, and internal energy, U, following the framework of Xu et al.[51]. Here, U is the sum of the potential and kinetic energies of all atoms and includes contributions from new surface formation, local structural relaxation, and residual elastic strain. The one-sided crack area, A, was determined by constructing surface meshes from atomic structures, extracting crack-tip coordinates at each position along the thickness direction, and integrating the incremental area from the initial edge-crack tip for one fracture surface. A linear fit was applied to the U–A relationship in the stable crack-propagation region after excluding the initial burst, and the slope, dU/dA, was defined as the crack-growth resistance.

The dU/dA obtained using this method reproduced the Griffith limit, 2γ, for Fe(001) cleavage

fracture. We therefore considered it an appropriate resistance metric for grain-boundary crack propagation without dislocation emission. In the original method of Xu et al., $d(W-U)/dA$, where W is the external work applied to the system, was used under NVT conditions to evaluate dissipated energy, which is suitable for plastic work associated with dislocation emission and slip[51]. However, when this metric was applied to cleavage fracture without plastic work, it gave values far below 2γ; therefore, it was not used in this study. Similar behaviour has also been reported in analyses using empirical interatomic potentials[53,54].

The static grain-boundary strengthening effect of carbon was evaluated as its contribution to the Rice–Wang-type ideal work of separation. Specifically, for the grain-boundary regions that actually fractured during crack propagation, we extracted the pre-fracture structure before strain loading and the post-fracture structure separated into two free surfaces after crack propagation. The work of separation was then calculated from the energy difference between these structures. The atomic structures used for this evaluation are shown in Supplementary Note 5. The works of separation for clean and carbon-segregated grain boundaries were denoted W_{sep}^{0} and $W_{\mathrm{sep}}^{\mathrm{C}}$, respectively, and their difference, $\Delta W_{\mathrm{sep}}^{\mathrm{C}} = W_{\mathrm{sep}}^{\mathrm{C}} - W_{\mathrm{sep}}^{0}$, was defined as the static Rice–Wang-type contribution of carbon. This evaluation represents the contribution to the static ideal work of separation based on atomic structures before and after fracture and does not include dynamic contributions arising from carbon rearrangement or Fe–C bond reconfiguration during crack propagation.

Atomistic analysis of DBR

To clarify the dynamic behaviour of carbon during crack propagation, we analysed the coordination number, Voronoi volume, displacement, and local carbon concentration near the crack tip. These analyses were performed using OVITO[52]. Local crystal structures were identified using polyhedral template matching[55]. Atomic volumes were calculated by Voronoi tessellation. Coordination numbers were evaluated by defining bonds using a cutoff distance of 2.8 Å, corresponding to the first-neighbour distance, and counting the number of bonds connected to the target atom. This setting gives a coordination number of 6 for carbon at octahedral sites in bulk α-Fe, consistent with the known crystallographic coordination. These descriptors were calculated at each deformation step and analysed as functions of strain to quantify local structural changes and bond reconfiguration during crack propagation.

Data availability

The final PACE interatomic potential developed in this study is publicly available at https://github.com/KazumaIto0810/Fe-C_PACE. The training dataset used to construct the potential is not publicly available because of intellectual property restrictions. Source data for the figures and representative atomic structures are available from the corresponding author upon reasonable request.

Code availability

The simulations and potential training used publicly available software packages, including DeePMD-kit[40], LAMMPS[39] and Pacemaker[27]. GeNNIP4MD[26], which was used to construct the training dataset, is proprietary software and is not open-source. Access to GeNNIP4MD may be provided upon reasonable request, subject to approval by Fujitsu Limited. Requests should be directed to fj-mi-tech-contact@dl.jp.fujitsu.com. Custom scripts used for post-processing are available from the corresponding author upon reasonable request.

Acknowledgments

This work used computational resources of the Supercomputer Fugaku provided by Riken through the HPCI System Research Project (Project IDs: hp230272, hp240280, hp250310). This work was partly supported by Accompanying User Support Program (【23Z-03, 23Z-05, 24H1-01】, Support content:【porting of application program, execution performance tuning】) performed by Research Organization for Information Science and Technology.

Funding statement

This research received no external financial funding.

Author contributions

K.I. conceived the study, developed and validated the Fe–C MLIP, performed the simulations, analysed the data, prepared the figures and wrote the original draft. N.M. and Y.Y. developed software used for potential development. T.O. reviewed and edited the manuscript. All authors discussed the results and commented on the manuscript.

Competing interests

The authors declare no competing interests.

References

1 Yu, H. *et al.* Hydrogen Embrittlement as a Conspicuous Material Challenge─Comprehensive Review and Future Directions. *Chem. Rev.* **124**, 6271-6392 (2024). https://doi.org/10.1021/acs.chemrev.3c00624

2 Okada, K., Watase, Y., Park, M.-h., Tsuzaki, K. & Shibata, A. Origin of the trade-off relationship between tensile strength and hydrogen embrittlement resistance. *Acta Mater.* **303**, 121683 (2026). https://doi.org/10.1016/j.actamat.2025.121683

3 Sun, B. *et al.* Chemical heterogeneity enhances hydrogen resistance in high-strength steels. *Nat. Mater.* **20**, 1629-1634 (2021). https://doi.org/10.1038/s41563-021-01050-y

4 Hachet, G. *et al.* Protection of metal interfaces against hydrogen-assisted cracking. *Nat. Commun.* **16**, 11032 (2025). https://doi.org/10.1038/s41467-025-67310-6

5 Razmpoosh, M. H., DiGiovanni, C., Zhou, Y. N. & Biro, E. Pathway to understand liquid metal embrittlement (LME) in Fe-Zn couple: From fundamentals toward application. *Prog. Mater. Sci.* **121**, 100798 (2021). https://doi.org/10.1016/j.pmatsci.2021.100798

6 Ikeda, Y. *et al.* Early stages of liquid-metal embrittlement in an advanced high-strength steel. *Mater. Today Adv.* **13**, 100196 (2022). https://doi.org/10.1016/j.mtadv.2021.100196

7 Yamaguchi, M., Tsuru, T., Itakura, M. & Abe, E. Atomistic weak interaction criterion for the specificity of liquid metal embrittlement. *Sci. Rep.* **12**, 10886 (2022). https://doi.org/10.1038/s41598-022-10593-2

8 Gong, P. *et al.* Hydrogen embrittlement mechanisms in advanced high strength steel. *Acta Mater.* **223**, 117488 (2022). https://doi.org/10.1016/j.actamat.2021.117488

9 Pineau, A., Benzerga, A. A. & Pardoen, T. Failure of metals I: Brittle and ductile fracture. *Acta Mater.* **107**, 424-483 (2016). https://doi.org/10.1016/j.actamat.2015.12.034

10 Ritchie, R. O. The conflicts between strength and toughness. *Nat. Mater.* **10**, 817-822 (2011). https://doi.org/10.1038/nmat3115

11 Orowan, E. Fracture and strength of solids. *Rep. Prog. Phys.* **12**, 185-232 (1949).

12 Irwin, G. R. Fracture dynamics. *Fracturing of metals* (1947).

13 Yamaguchi, M. & Kameda, J. Multiscale thermodynamic analysis on fracture toughness loss induced by solute segregation in steel. *Philos. Mag.* **94**, 2131-2149 (2014). https://doi.org/10.1080/14786435.2014.906757

14 Rice, J. R. & Wang, J.-S. Embrittlement of interfaces by solute segregation. *Mater. Sci. Eng., A* **107**, 23-40 (1989). https://doi.org/10.1016/0921-5093(89)90372-9

15 Wu, R., Freeman, A. J. & Olson, G. B. First Principles Determination of the Effects of Phosphorus and Boron on Iron Grain Boundary Cohesion. *Science* **265**, 376 (1994). https://doi.org/10.1126/science.265.5170.376

16 Lejček, P., Šob, M. & Paidar, V. Interfacial segregation and grain boundary embrittlement: An overview and critical assessment of experimental data and calculated results. *Prog. Mater. Sci.* **87**, 83-139 (2017). https://doi.org/10.1016/j.pmatsci.2016.11.001

17 Yamaguchi, M. First-Principles Study on the Grain Boundary Embrittlement of Metals by Solute Segregation: Part I. Iron (Fe)-Solute (B, C, P, and S) Systems. *Metall. Mater. Trans. A* **42**, 319-329 (2011). https://doi.org/10.1007/s11661-010-0381-5

18 Jokl, M. L., Vitek, V. & McMahon, C. J. A microscopic theory of brittle fracture in deformable solids: A relation between ideal work to fracture and plastic work. *Acta Metall.* **28**, 1479-1488 (1980). https://doi.org/10.1016/0001-6160(80)90048-6

19 Jokl, M., Kameda, J., McMahon, C. & Vitek, V. Solute segregation and intergranular brittle fracture in steels. *Met. Sci.* **14**, 375-384 (1980).

20 Araki, S. *et al.* Effect of Low Temperature Aging on Hall-Petch Coefficient in Ferritic Steels Containing a Small Amount of Carbon and Nitrogen. *ISIJ Int.* **58**, 1920-1926 (2018). https://doi.org/10.2355/isijinternational.ISIJINT-2018-130

21 Tanaka, M. *et al.* Effects of Ni and Mn on brittle-to-ductile transition in ultralow-carbon steels. *Mater. Sci. Eng., A* **682**, 370-375 (2017). https://doi.org/10.1016/j.msea.2016.11.045

22 Tanaka, M. *et al.* Effect of Mn Addition on a Brittle-to-Ductile Transition in Ferritic Steels. *Tetsu-to-Hagane* **100**, 1267-1273 (2014). https://doi.org/10.2355/tetsutohagane.100.1267

23 Miyazawa, N., Hakamada, M. & Mabuchi, M. Atomic bond-breaking behaviour during grain boundary fracture in a C-segregated Fe grain boundary. *Philos. Mag. Lett.* **97**, 311-319 (2017). https://doi.org/10.1080/09500839.2017.1354134

24 Ito, K., Yokoi, T., Hyodo, K. & Mori, H. Machine learning interatomic potential with DFT accuracy for general grain boundaries in α-Fe. *npj Comput. Mater.* **10**, 255 (2024). https://doi.org/10.1038/s41524-024-01451-y

25 Frenkel, D. & Smit, B. *Understanding molecular simulation: from algorithms to applications*. (elsevier, 2023).

26 Matsumura, N. *et al.* Generator of Neural Network Potential for Molecular Dynamics: Constructing Robust and Accurate Potentials with Active Learning for Nanosecond-Scale Simulations. *Journal of Chemical Theory and Computation* **21**, 3832-3846 (2025). https://doi.org/10.1021/acs.jctc.4c01613

27 Bochkarev, A. *et al.* Efficient parametrization of the atomic cluster expansion. *Phys. Rev. Mater.* **6**, 013804 (2022). https://doi.org/10.1103/PhysRevMaterials.6.013804

28 Lysogorskiy, Y. *et al.* Performant implementation of the atomic cluster expansion (PACE) and application to copper and silicon. *npj Comput. Mater.* **7**, 97 (2021). https://doi.org/10.1038/s41524-021-00559-9

29 Meng, F.-S. *et al.* A highly transferable and efficient machine learning interatomic potentials study of α-Fe–C binary system. *Acta Mater.* **281**, 120408 (2024). https://doi.org/10.1016/j.actamat.2024.120408

30 Podryabinkin, E., Garifullin, K., Shapeev, A. & Novikov, I. MLIP-3: Active learning on atomic environments with moment tensor potentials. *The Journal of Chemical Physics* **159**, 084112 (2023). https://doi.org/10.1063/5.0155887

31 Zhou, X., Foster, M. E., Ronevich, J. A. & San Marchi, C. W. Review and construction of interatomic potentials for molecular dynamics studies of hydrogen embrittlement in Fe─C based steels. *J Comput Chem* **41**, 1299-1309 (2020). https://doi.org/10.1002/jcc.26176

32 Liyanage, L. S. I. *et al.* Structural, elastic, and thermal properties of cementite (${¥mathrm{Fe}}_{3}C$) calculated using a modified embedded atom method. *Phys. Rev. B* **89**, 094102 (2014). https://doi.org/10.1103/PhysRevB.89.094102

33 Li, C., Lu, S., Divinski, S. & Vitos, L. Theoretical and experimental grain boundary energies in body-centered cubic metals. *Acta Mater.* **255**, 119074 (2023). https://doi.org/10.1016/j.actamat.2023.119074

34 Yanagimoto, F., He, T. & Shibanuma, K. The state-of-art in studies on brittle crack arrest in steel. *Eng. Fract. Mech.* **323**, 111132 (2025). https://doi.org/10.1016/j.engfracmech.2025.111132

35 Kimura, H. Intergranular Fracture in BCC Metals. *Trans. Jpn. Inst. Met.* **29**, 521-539 (1988). https://doi.org/10.2320/matertrans1960.29.521

36 Wang, Z. *et al.* Solving oxygen embrittlement of refractory high-entropy alloy via grain boundary engineering. *Mater. Today* **54**, 83-89 (2022). https://doi.org/10.1016/j.mattod.2022.02.006

37 Reiners-Sakic, A., Reichmann, A., Dösinger, C., Romaner, L. & Holec, D. Interstitials as a key ingredient for P segregation to grain boundaries in polycrystalline α-Fe. *Scr. Mater.* **268**, 116864 (2025). https://doi.org/10.1016/j.scriptamat.2025.116864

38 Ito, K. *et al.* Predicting hydrogen diffusion in nickel–manganese random alloys using

machine learning interatomic potentials. *Commun. Mater.* **6**, 195 (2025). https://doi.org/10.1038/s43246-025-00924-x

39 Plimpton, S. Fast Parallel Algorithms for Short-Range Molecular Dynamics. *J. Comput. Phys.* **117**, 1-19 (1995). https://doi.org/10.1006/jcph.1995.1039

40 Zhang, Y. *et al.* DP-GEN: A concurrent learning platform for the generation of reliable deep learning based potential energy models. *Comput. Phys. Commun.* **253**, 107206 (2020). https://doi.org/10.1016/j.cpc.2020.107206

41 Kresse, G. & Joubert, D. From ultrasoft pseudopotentials to the projector augmented-wave method. *Phys. Rev. B* **59**, 1758-1775 (1999). https://doi.org/10.1103/PhysRevB.59.1758

42 Kresse, G. & Furthmüller, J. Efficient iterative schemes for ab initio total-energy calculations using a plane-wave basis set. *Phys. Rev. B* **54**, 11169-11186 (1996). https://doi.org/10.1103/PhysRevB.54.11169

43 Ito, K., Yokoi, T., Hyodo, K. & Mori, H. Transferability of machine-learning interatomic potential to α-Fe nanocrystalline deformation. *Int. J. Mech. Sci.* **291-292**, 110132 (2025). https://doi.org/10.1016/j.ijmecsci.2025.110132

44 Ito, K., Otaki, T., Yokoi, T., Hyodo, K. & Mori, H. Machine learning interatomic potential reveals hydrogen embrittlement origins at general grain boundaries in α-iron. *Commun. Mater.* **7**, 30 (2025). https://doi.org/10.1038/s43246-025-01042-4

45 Kadota, N. *et al.* Room-temperature plastic deformation of single crystals of cementite investigated by micropillar compression. *Acta Mater.* **304**, 121759 (2026). https://doi.org/10.1016/j.actamat.2025.121759

46 Ito, K. Fast and accurate Fe-H machine-learning interatomic potential for elucidating hydrogen embrittlement mechanisms. *arXiv preprint arXiv:2512.22934* (2025).

47 Shuang, F. *et al.* Modeling extensive defects in metals through classical potential-guided sampling and automated configuration reconstruction. *npj Comput. Mater.* **11**, 118 (2025). https://doi.org/10.1038/s41524-025-01599-1

48 Ito, K. Fast and accurate Fe–H machine-learning interatomic potential for elucidating hydrogen embrittlement mechanisms. *Int. J. Hydrog. Energy* **242**, 155600 (2026). https://doi.org/10.1016/j.ijhydene.2026.155600

49 Freitas, R., Asta, M. & de Koning, M. Nonequilibrium free-energy calculation of solids using LAMMPS. *Comput. Mater. Sci.* **112**, 333-341 (2016). https://doi.org/10.1016/j.commatsci.2015.10.050

50 Hirel, P. Atomsk: A tool for manipulating and converting atomic data files. *Comput. Phys. Commun.* **197**, 212-219 (2015). https://doi.org/10.1016/j.cpc.2015.07.012

51 Xu, G. Q. & Demkowicz, M. J. Computing critical energy release rates for fracture in atomistic simulations. *Comput. Mater. Sci.* **181**, 109738 (2020). https://doi.org/10.1016/j.commatsci.2020.109738

52 Stukowski, A. Visualization and analysis of atomistic simulation data with OVITO–the Open

Visualization Tool. *Model. Simul. Mater. Sci. Eng.* **18**, 015012 (2010). https://doi.org/10.1088/0965-0393/18/1/015012

53 Lin, P.-d., Nie, J.-f., Cui, S.-g. & Lu, Y.-p. Molecular dynamics study on the ductile-to-brittle transition in W-Re alloy systems. *Acta Mater.* **285**, 120684 (2025). https://doi.org/10.1016/j.actamat.2024.120684

54 Barik, R. K., Jayasree, T., Biswal, S., Ghosh, A. & Chakrabarti, D. Investigating the ductile to brittle transition phenomenon in binary Fe-Ni systems using molecular dynamics simulation. *J. Mech. Phys. Solids* **187**, 105624 (2024). https://doi.org/10.1016/j.jmps.2024.105624

55 Larsen, P. M., Schmidt, S. & Schiøtz, J. Robust structural identification via polyhedral template matching. *Model. Simul. Mater. Sci. Eng.* **24**, 055007 (2016). https://doi.org/10.1088/0965-0393/24/5/055007

Supplementary Files

This is a list of supplementary files associated with this preprint. Click to download.

- SupplementaryInformation20260527.docx
- SupplementaryVideos1.mp4
- SupplementaryVideos2.mp4